AGU PUBLICATIONS

JGR

Journal of Geophysical Research: Oceans

RESEARCH ARTICLE
10.1002/2015JC011167

Special Section:
Forum for Arctic Modeling and Observing Synthesis (FAMOS): Results and Synthesis of Coordinated Experiments

Future change in ocean productivity: Is the Arctic the new Atlantic?

A. Yool[1], E. E. Popova[1], and A. C. Coward[1]

[1]National Oceanography Centre, University of Southampton, Southampton, UK

Abstract One of the most characteristic features in ocean productivity is the North Atlantic spring bloom. Responding to seasonal increases in irradiance and stratification, surface phytopopulations rise significantly, a pattern that visibly tracks poleward into summer. While blooms also occur in the Arctic Ocean, they are constrained by the sea-ice and strong vertical stratification that characterize this region. However, Arctic sea-ice is currently declining, and forecasts suggest this may lead to completely ice-free summers by the mid-21st century. Such change may open the Arctic up to Atlantic-style spring blooms, and do so at the same time as Atlantic productivity is threatened by climate change-driven ocean stratification. Here we use low and high-resolution instances of a coupled ocean-biogeochemistry model, NEMO-MEDUSA, to investigate productivity. Drivers of present-day patterns are identified, and changes in these across a climate change scenario (IPCC RCP 8.5) are analyzed. We find a globally significant decline in North Atlantic productivity ($> -20\%$) by 2100, and a correspondingly significant rise in the Arctic ($> +50\%$). However, rather than the future Arctic coming to resemble the current Atlantic, both regions are instead transitioning to a common, low nutrient regime. The North Pacific provides a counterexample where nutrients remain high and productivity increases with elevated temperature. These responses to climate change in the Atlantic and Arctic are common between model resolutions, suggesting an independence from resolution for key impacts. However, some responses, such as those in the North Pacific, differ between the simulations, suggesting the reverse and supporting the drive to more fine-scale resolutions.

Key Points:
- Across 21st century, N. Atlantic productivity significantly declines while increasing in the Arctic
- Despite disparate climate change responses, regions share underlying convergence in nutrient status
- Results broadly consistent between different model resolutions though they differ in subbasin detail

Supporting Information:
- Supporting Information S1
- Supporting Information S2

Correspondence to:
A. Yool,
axy@noc.ac.uk

Citation:
Yool, A., E. E. Popova, and A. C. Coward (2015), Future change in ocean productivity: Is the Arctic the new Atlantic?, *J. Geophys. Res. Oceans*, *120*, 7771–7790, doi:10.1002/2015JC011167.

Received 29 JUL 2015
Accepted 20 OCT 2015
Accepted article online 26 OCT 2015
Published online 12 DEC 2015
Corrected 5 JAN 2016

This article was corrected on 5 JAN 2016. See the end of the full text for details.

1. Introduction

Productivity of planktonic autotrophs in the ocean is principally regulated by the availability of energy and matter for biosynthesis. Energy, in the form of light, varies both in terms of space, latitude, and depth, and in terms of time, diel, and seasonal. Matter, typically nitrogen, phosphorus, and iron nutrients, varies in a more complex pattern spatially, although depth is still key, and generally only in a seasonal sense temporally. A key linkage between both is the extent of turbulent surface mixing that defines the so-called mixed layer depth (MLD). This governs the depth to which plankton are mixed, and thus the average light field they experience, and the depth from which nutrients resupply surface waters. Other factors, such as the abundance of grazing heterotrophs, also play a role, but the interplay of light and nutrient availability is a key factor in the occurrence of the canonical productivity feature, the spring bloom [*Heinrich*, 1962].

Spring blooms are a widespread phenomenon across the ocean from the subtropics to polar waters. As the name implies, they typically occur during the onset of spring, though local conditions can push this timing slightly earlier (late winter) or later (early summer). As a well-known feature of aquatic systems with a fundamental role in driving food webs, spring blooms, and the factors which underpin and regulate them, have been studied for decades [e.g., *Gran and Braarud*, 1935; *Riley*, 1942; *Sverdrup*, 1953; *Hulburt et al.*, 1960; *Pingree et al.*, 1975; *Dagg and Turner*, 1982; *Townsend et al.*, 1992; *Siegel et al.*, 2002; *Cole et al.*, 2012].

Classically, the mechanism for their occurrence involves prebloom conditioning of surface waters by deep winter mixing that replenishes their nutrient concentrations. This is followed in spring by the shoaling of mixed layer depth by heat flux-driven stratification of the water column (but see below for the Arctic), which in turn leads to phytoplankton experiencing light levels that, on average, permit photosynthesis to exceed respiration and trigger exponential growth [*Sverdrup*, 1953]. However, this classic viewpoint does not describe a universal mechanism, and much work has picked apart its details. For instance, in oligotrophic gyre regions, where surface nutrient concentrations are low for much of the year, the *deepening* mixing in

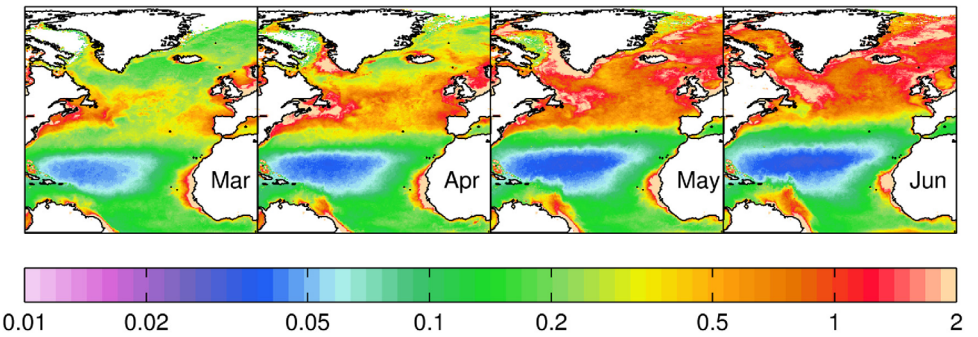

Figure 1. Northward progression of the spring bloom in the North Atlantic. The plots show four spring months from a decadal climatology of SeaWiFS chlorophyll observations. Chlorophyll is shown on a logarithmic scale in units of mg chl m^{-3}.

late winter itself triggers the blooms [*DuRand et al*., 2001; *Siegel et al*., 2002] And the distinction between a *mixed* layer, as diagnosed from stratification, and a *mixing* layer, as diagnosed from turbulent kinetic energy, can be important in defining the average light (and grazing) experienced down the water column [*Boss and Behrenfeld*, 2010; *Taylor and Ferrari*, 2011]. Nevertheless, the interplay between light, nutrients, and mixing still plays the dominant role in triggering spring blooms.

Largely for reasons of proximity and convenience, the spring bloom in the North Atlantic (poleward of 45°N) has been extensively studied since the earliest days of oceanography [*Gran and Braarud*, 1935]. Starting around March, the bloom begins in coastal regions off Western Europe and North America, before spreading across the deep Atlantic and then northward, with the bloom reaching the Atlantic gateway of the Greenland-Iceland-Norway (GIN) Sea by June. Figure 1 illustrates this, showing monthly averages of surface chlorophyll in the North Atlantic for March to June from a decades worth of satellite-derived observations. Concentrations of surface chlorophyll in this area can rise from around 0.1 to more than 2.0 mg chl m^{-3} at the height of the bloom.

As Figure 1 hints, the progression of the North Atlantic bloom into the Arctic Ocean is complicated by the presence of sea-ice in the latter (note the white "missing data" at the top of the plot). Reaching several meters in thickness in parts of the Arctic, this sea-ice blocks the penetration of light to underlying waters, and an already high albedo can be further increased if it is additionally covered in snow. While a large section of the Arctic has historically had a permanent cover of ice (7×10^6 km^2), this is bordered by a marginal ice zone which seasonally sees ice melt during the summer months and growth during the winter (9×10^6 km^2) [*Serreze et al*., 2007]. In this marginal area, where ice is much thinner and can be fractured by leads at scales below the resolution of satellite sensors, the linked phenomena of under-ice [*Mundy et al*., 2009] and ice-edge blooms [*Sakshaug and Skjoldal*, 1989] have been documented. Viewed from satellite platforms, the latter occur ubiquitously across the Arctic as sea-ice retreats [*Perrette et al*., 2011], and, though more difficult to observe synoptically, the former would also be expected to occur widely. Note that sea-ice plays a further role for Arctic blooms since seasonal stratification in this region is primarily driven by buoyancy from the freshwater produced when it melts rather than from solar heating.

As an aside, spring blooms are counterpointed in the seasonal cycle by autumn blooms [e.g., *Zingone et al*., 1995]. These are somewhat mirror-image blooms in that they are driven instead by the breakdown of stratification and the reintroduction of nutrients to depleted upper mixed layer at a point in the season when light is still relatively high [*Findlay et al*., 2006]. Though recognition of these has increased, including in the Arctic [*Ardyna et al*., 2014], they are not considered further here.

Driven by anthropogenic climate change—amplified within the Arctic [*Serreze and Barry*, 2011]—the ongoing decline in permanent sea-ice cover is now well established [*Serreze et al*., 2007], potentially at a rate faster than that estimated by many climate models [*Mahlstein and Knutti*, 2011]. The fate of Arctic sea-ice will primarily depend on human emissions of greenhouse gases, but it is widely anticipated that the Arctic will become seasonally ice free within the 21st century, potentially within the first half of the century [*Wang and Overland*, 2009]. Under such circumstances, where the Arctic has no permanent ice cover, what could happen to the spring bloom?

Previous studies have considered future trends in Arctic Ocean chlorophyll and primary production [e.g., *Vancoppenolle et al*., 2013; *Popova et al*., 2014], but they have typically focused on mean annual values (sometimes out of necessity) rather than seasonal variability. This may overlook facets of the Arctic ecosystem, for instance, higher trophic levels can be adapted to a particular regime—timing and magnitude—of bloom variability.

Here we use an ocean model run at two different resolutions to investigate the fates of both the North Atlantic and Arctic blooms under a strong climate warming scenario. We focus initially on the temporal progression of change across the 21st century, before examining the underlying factors that regulate ocean productivity between these two basins. Change during this period is also compared with that in the corresponding region of the North Pacific, an area that may otherwise be expected to have a similar fate. Resolution is examined here because of the role of spatial scale in the representation of important hydrographic features, such as boundary currents, that influence wider ocean circulation. The simulations used include a medium resolution instance comparable to that used in Coupled Model Intercomparison Project 5 (CMIP5) to inform Intergovernmental Panel on Climate Change (IPCC) Assessment Report 5 (AR5) [*Flato et al*., 2013], and a high-resolution instance comparable to that anticipated to be used in CMIP6 for IPCC AR6. As well as covering this CMIP evolution, this span of resolution takes the ocean model from effectively ignoring mesoscale features to permitting them, potentially with consequences for Arctic blooms and biogeochemistry.

2. Methods

2.1. Model Physics

The physical framework used throughout this work is the Nucleus for European Modelling of the Ocean (NEMO) model [*Madec*, 2008]. This framework is composed of an ocean general circulation model, Océan PArallélisé version 9 (OPA9) [*Madec et al*., 1998; *Madec*, 2008], coupled to a sea-ice model, Louvain-la-Neuve Ice Model version 2 (LIM2) [*Timmermann et al*., 2005]. OPA9 is a primitive equation model and is configured in this work at global scale and at two grid resolutions:

1. A "medium resolution" instance at approximately 1° horizontal resolution (362 × 292 grid cells), with a focusing of resolution around the equator to improve the representation of equatorial upwelling, and average grid cell resolutions of 73.4 km (25.0 → 111.2 km) globally and 50.0 km (27.8 → 62.4 km) in the Arctic (poleward of 70°); vertical space here is divided into 64 levels, which increase in thickness with depth, from approximately 6 m at the surface to 250 m at 6000 m; ocean time step of 60 min.
2. A "high-resolution" instance at approximately 0.25° horizontal resolution (1442 × 1021 grid cells), and average grid cell resolutions of 19.0 km (6.0 → 27.8 km) globally and 12.5 km (6.8 → 15.4 km) in the Arctic (poleward of 70°); vertical space here is divided into 75 levels, which increase in thickness with depth, from approximately 1 m at the surface to 200 m at 6000 m; ocean time step of 24 min.

Both instances utilize a tripolar grid configuration in which the Southern Hemisphere has a pole in the conventional location, but in which the Northern Hemisphere has poles located in Canada and Siberia that distort the grid to avoid a polar singularity within the ocean domain (i.e., a single point at which all meridians converge). To improve the representation of bottom topography and circulation at depth, OPA9 allows for partial level thickness cells at the seafloor. Vertical mixing is parameterized using the turbulent kinetic energy (TKE) scheme of *Gaspar et al*. [1990], and incorporates the modifications of *Madec* [2008].

The sea-ice submodel, LIM2, is based upon a viscous-plastic ice rheology [*Hibler*, 1979] with three layer (two × ice, one × snow) thermodynamics [*Semtner*, 1976] (with updated physical processes per *Timmermann et al*. [2005, and references therein]). NEMO's sea-ice is coupled to its ocean every five ocean time steps through a nonlinear quadratic drag law of the shear between ocean surface and sea-ice velocity [*Timmermann et al*., 2005]. Freshwater exchange between the ocean and sea-ice is calculated from ice formation/melting and precipitation [*Fichefet and Morales Maqueda*, 1997], while the heat flux between the ocean and sea-ice is proportional to the friction velocity at the ice-ocean interface and the departure in temperature from the salinity-dependent freezing point. Solar radiation can penetrate sea-ice that is not covered by snow, and is dissipated within the ice [*Fichefet and Morales Maqueda*, 1997].

Simulations using the same medium resolution instance of NEMO have previously been published by *Yool et al*. [2013b] and *Popova et al*. [2014], and further details concerning NEMO can be found there. Because of the ongoing development cycle of the model, the medium resolution instance used NEMO v3.2, while the

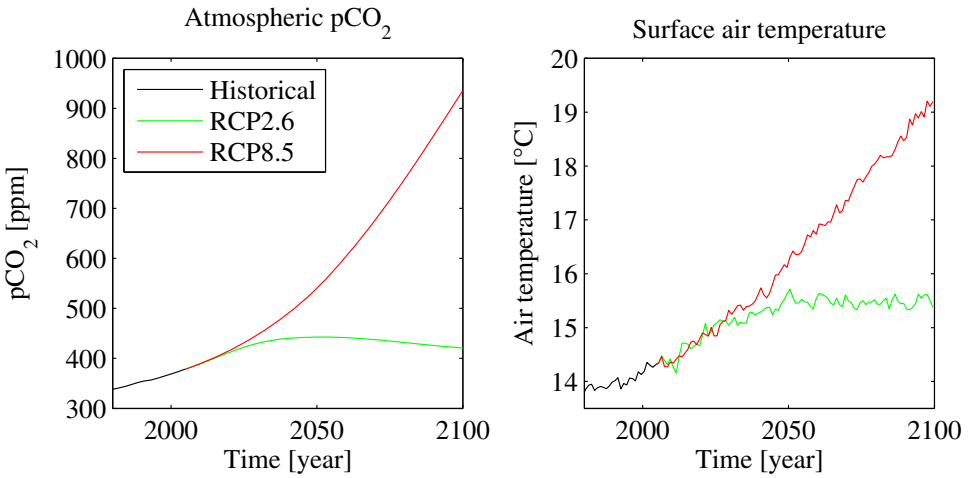

Figure 2. (**left**) Atmospheric pCO_2 forcing, showing the historical period (black), the "business-as-usual" scenario, RCP 8.5, used in this work (red), and a strong mitigation scenario, RCP 2.6, for comparison (green). (right) The resulting globally averaged surface air temperature for the pCO_2 scenarios. The latter is drawn from the HadGEM2-ES model that provided the surface forcing output used in this work.

high-resolution instance used NEMO v3.4, although parameter values and options chosen were kept the same where possible.

2.2. Model Biogeochemistry

The biogeochemistry component used in this work is the Model of Ecosystem Dynamics, nutrient Utilization, Sequestration and Acidification (MEDUSA-2, henceforth MEDUSA) [*Yool et al*., 2013a], an "intermediate complexity" model of the plankton ecosystem founded on the oceanic nitrogen cycle. Though simplified, MEDUSA is designed to represent sufficient complexity for it to address the major feedbacks between ocean biogeochemical cycles and anthropogenic drivers such as climate change (CC) and ocean acidification (OA). MEDUSA includes the elemental cycles of nitrogen, carbon, oxygen, silicon, and iron, and links these in a dual size-class nutrient-phytoplankton-zooplankton-detritus plankton ecosystem model. This includes nitrogen, silicon, and iron nutrients, "small" (nanophytoplankton and microzooplankton) and "large" (microphytoplankton and mesozooplankton) living components, and two pools of sinking detrital material. "Large" phytoplankton are assumed to be synonymous with diatoms in MEDUSA, and have a requirement for silicon [*Mongin et al*., 2006]. "Small" detritus is assumed to be slow sinking and is modeled explicitly, while "large" detritus is assumed to be fast sinking and is modeled implicitly using a variant of the *Armstrong et al*. [2002] ballast model [*Klaas and Archer*, 2002; *Dunne et al*., 2007]. Here the ballast model is framed using biogenic fluxes of opal [*Mongin et al*., 2006] and calcium carbonate [*Ridgwell et al*., 2007]. MEDUSA includes air-sea exchanges of carbon dioxide and oxygen, and aoelian deposition and sedimentary inputs of iron, but does not include any riverine inputs of biogeochemical properties.

MEDUSA is extensively described and validated in *Yool et al*. [2013a], and has participated in several model intercomparison exercises [*Popova et al*., 2012; *Kwiatkowski et al*., 2014].

2.3. Simulations

Both resolution instances of NEMO used here are forced at the ocean surface using output from a simulation of the HadGEM2-ES Earth system model developed by the UK Meteorological Office (UKMO). This simulation was performed as part of the UKMO's input to the Coupled Model Intercomparison Project 5 (CMIP5) [*Jones et al*., 2011] and Assessment Report 5 (AR5) of the Intergovernmental Panel on Climate Change (IPCC). The simulation ran from start-1860 to end-2005 under historical atmospheric pCO_2 concentrations, and then from start-2006 to end-2099 under the IPCC RCP 8.5 pathway. RCP 8.5 is a scenario in which CO_2 emissions rise throughout the 21st century, leading to approximately 8.5 W m^{-2} of additional radiative forcing by the end of the century. Figure 2 shows the atmospheric pCO_2 in this scenario, together with the resulting globally averaged surface air temperature (as simulated by HadGEM2-ES). An unexamined low scenario, RCP 2.6, is shown here to illustrate the broad range of scenarios considered by the IPCC.

The model output from this simulation of HadGEM2-ES was processed into forcing fields of the same properties and frequencies as that of reanalysis data sets such as DFS4.1 [*DRAKKAR Group*, 2007] and CORE2

[*Large and Yeager*, 2009], namely monthly for precipitation (rain, snow, runoff), daily for radiation (downwelling short and long wave), and 6 hourly for turbulent variables (air temperature, humidity, and wind velocity). Further details can be found in *Yool et al*. [2013a].

The medium resolution instance of NEMO was initialized in year 1860 using temperature and salinity fields from the same HadGEM2-ES simulation at the same time point. To decrease drift in NEMO, sea surface salinity (SSS) was relaxed (with a time scale of 30 days) toward that from HadGEM2-ES. The simulation's freshwater budget was also corrected for imbalances between forced (downward) precipitation and calculated (upward) evaporation. Ocean biogeochemistry was initialized from the World Ocean Atlas 2009 (WOA09) [*Garcia et al*., 2010a] (dissolved inorganic nitrogen, silicic acid, dissolved oxygen), a long-term iron cycle simulation [*Dutkiewicz et al*., 2005] (total iron), and the Global Data Analysis Project (GLODAP) [*Key et al*., 2004] (dissolved inorganic carbon and total alkalinity). It was assumed that GLODAP's preindustrial DIC field is approximately valid for 1860, and regional lacunae, such as the Arctic Ocean, were filled using localized multiple linear regressions (MLRs) of WOA09 and GLODAP. Plankton and detrital state variables were initialized at nominal, low values. The model was then integrated to end-2099 under the surface forcing described above, and the corresponding time history of pCO_2 concentrations. Again, further details can be found in *Yool et al*. [2013a, 2013b].

Because of its high computational cost, the high-resolution instance of NEMO was instead initialized in year 1975 from a regridded physical and biogeochemical state from a medium resolution instance of NEMO following the same initialization protocol described above. This was then simulated to end-2099 in the same manner as described above.

In the case of both instances of the model, the simulations produced monthly average model output (= 30 days; based on a 360 day year), and this frequency is used here throughout our analysis.

2.4. Validation

As noted previously, one of the key motivations for increased physical model resolution is improvement in the representation of circulation features. Particularly so in the surface ocean, where biogeochemical cycles are the most active and responsive to features such as boundary currents, upwelling zones, and mesoscale features. Figure 3 shows surface current velocities in the Atlantic Ocean for both NEMO resolutions used here, together with a corresponding satellite-derived observational data set, the Aviso geostrophic velocity product [*AVISO*, 2014]. This product calculates sea surface geostrophic velocities from the Absolute Dynamic Topography (ADT). The ADT in turn is calculated by adding the Sea Level Anomaly to the Mean Dynamic Topography, which is the part of the Mean Sea Surface Height caused by permanent currents (i.e., Mean Sea Surface Height minus Geoid). The altimeter products were produced by Ssalto/Duacs and distributed by Aviso, with support from CNES (http://www.aviso.altimetry.fr.duacs). In each case here, the velocities shown are on the same scale, represent the decadal average for the period 2000–2009, and are derived from monthly average velocity fields. Note that the comparison is illustrative of general patterns and magnitudes only since the modeled period, 2000–2009, will not match that observed because the surface forcing is derived from a coupled model with its own modes of variability.

As would be expected, the high-resolution instance of NEMO is much more capable of representing current features of the North Atlantic Ocean than its medium resolution sibling. In particular, major currents such as the Gulf Stream, the Greenland Current, and the Labrador Current are generally well represented. Medium resolution NEMO, by contrast, can only resolve the basin's major currents in outline, and smears high-velocity regions into broad zones of less coherent flow. Nonetheless, high-resolution NEMO still poorly resolves a number of features and details of surface circulation. For instance, the Gulf Stream separation at Cape Hatteras is stalled to a more northerly location, the flow around the Grand Banks is largely displaced eastward, and the Azores Current is not clearly resolved. More generally, the model underestimates the spatial variability of surface currents. This underestimation extends also to the relatively quiescent gyre areas, where high-resolution NEMO, though eddy permitting, cannot resolve the observed background velocities driven by eddy activity. That this, deficiency is rooted in resolution is underscored by higher-resolution instances of NEMO [*Marzocchi et al*., 2015], which perform better in these regions through resolving eddies directly.

Note that, because of its cover of sea-ice, surface currents in the Arctic are not resolved in the Aviso product, and this region is not examined here. However, the distribution of sea-ice itself is well characterized by

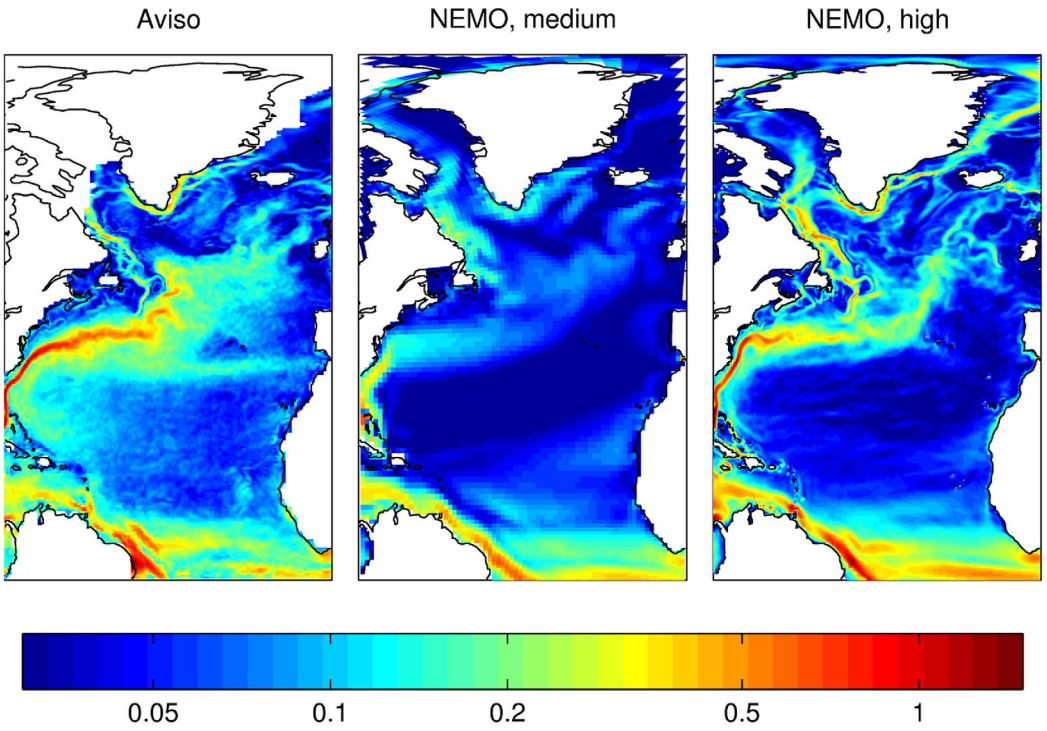

Figure 3. Averaged current velocity in the North Atlantic for the period 2000–2009 from the (left) Aviso product, (middle) medium resolution NEMO, and (right) high-resolution NEMO. Current velocity is in m s^{-1}, and is shown on a logarithmic scale to better illustrate both low and high-velocity regions. Note that velocity is shown on a logarithmic scale.

observations, and Figure 6 compares Arctic sea-ice extent for both instances of NEMO with the HadISST data set [*Rayner et al*., 2003]. As sea-ice has strong seasonal dynamics, its range is illustrated using monthly averages from March (maximum extent) and September (minimum extent) drawn from the period 2000–2009. In general, both model instances show relatively good agreement in terms of both sea-ice extent and concentration. At maximum extent, both similarly overestimate sea-ice in the Bering Sea and the Sea of Okhotsk, while underestimating its concentration within the Labrador Sea. At minimum extent, both models tend to overestimate the extent, but underestimate concentration, in the central Arctic, as well as overestimating sea-ice in the Canadian Archipelago. Comparing the model instances with one another, there is a general tendency for medium resolution NEMO to have greater, and excessive, sea-ice extent, most noticeably in September in the central Arctic, and also east of Greenland year round, but both generally perform similarly well. Figure 7 (see later) additionally shows a comparison of integrated sea-ice, both for HadISST and for the NSIDC data set [*Meier et al*., 2013]. While the specific patterns of interannual variability necessarily do not match (since the models are forced using output from a coupled model with its own interannual variability), the models are in agreement with the observed ranges of total sea-ice extent, both between seasons and between products.

In terms of ocean biogeochemistry, *Yool et al*. [2013a] describes an extended validation of medium resolution MEDUSA, including a cross validation with comparable CMIP5 models. Among other properties, this considers state variables such as nutrients, plankton, and dissolved gases, as well as key fluxes such as primary and export production, and uses these to examine geographical and seasonal performance. In general, MEDUSA reproduces the variables examined adequately across the board, albeit with discrepancies, some of which stem from deficiencies in NEMO. The most significant of these is an enhanced production of Antarctic Bottom Water that overventilates the deep Southern Ocean and produces discrepancies in the vertical profiles of nutrients and oxygen in this region.

As this previous validation used only medium resolution MEDUSA, Figure 4 compares [cf. *Yool et al*., 2013a] annual mean fields from both resolutions with corresponding observational fields of nutrients (World Ocean Atlas) [*Garcia et al*., 2010b], chlorophyll (SeaWiFS) [O'*Reilly et al*., 1998], and estimated primary production

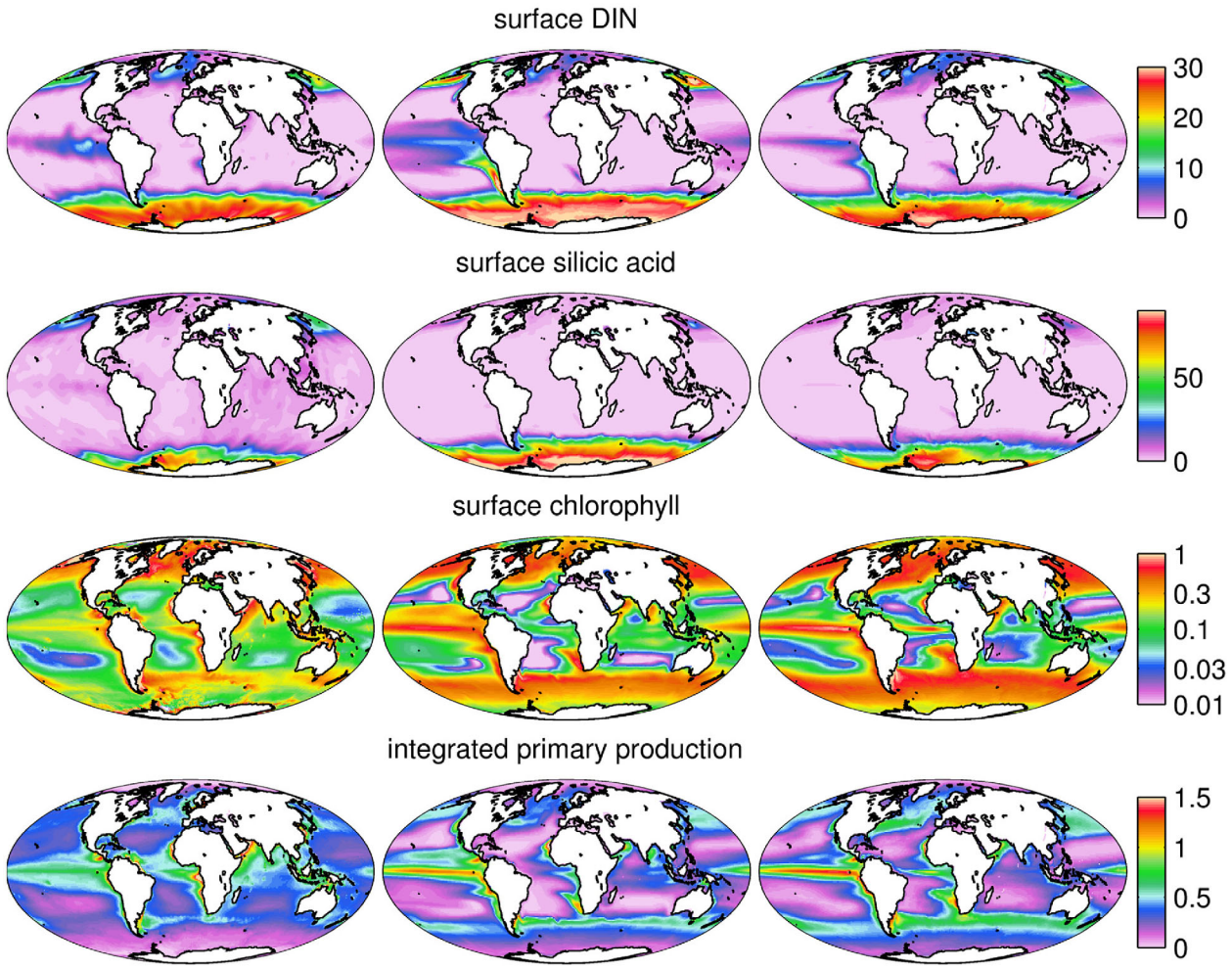

Figure 4. (left) Observational, (middle) medium resolution NEMO, and (right) high-resolution NEMO annual average fields of (row 1) surface DIN (mmol N m^{-3}), (row 2) surface silicic acid (mmol Si m^{-3}), (row 3) surface chlorophyll (mg chl m^{-3}), and (row 4) vertically integrated (full water column) primary production (g C m^{-2} d^{-1}). Average period is 2000–2009. Note that chlorophyll is shown on a logarithmic scale.

[*Behrenfeld and Falkowski*, 1997; *Carr et al.*, 2006; *Westberry et al.*, 2008]. For surface DIN distributions, both model resolutions reproduce some general patterns well (subpolar highs; subtropical lows) while representing others poorly (overestimated equatorial Pacific; underestimated North Atlantic). Silicic acid patterns in both instances show overestimates in the Southern Ocean, underestimates in the North Pacific Ocean, and an absence of low-level variability in the tropics and subtropics. As noted by *Yool et al.* [2013a], chlorophyll shows broad patterns of agreement, but also consistent biases in which modeled concentrations are higher where observed values are high (e.g., high latitudes; equatorial Pacific), and lower where they are low (e.g., oligotrophic gyres). In addition, there are more specific mismatches, such as elevated chlorophyll concentrations in both the Southern Ocean (especially its Pacific sector) and the North Pacific. Finally, and perhaps unsurprisingly, productivity follows these patterns in surface chlorophyll, though to a less extreme degree. However, despite these biases, modeled productivity generally follows the (estimated) observed patterns.

Regarding performance across model resolution more specifically, MEDUSA's skill is generally similar between the medium and high-resolution instances of NEMO, although the change in resolution has a noticeable impact. While there are locations where medium resolution MEDUSA is more congruent with observations, high-resolution MEDUSA is generally superior. This is most clearly the case with surface nutrients, in particular in the Southern Ocean, where the representation of vertical physical processes is improved and results in much lower positive biases than those mentioned earlier [*Yool et al.*, 2013a]. Chlorophyll also shows some improvements, but both instances of MEDUSA have the marked, and shared,

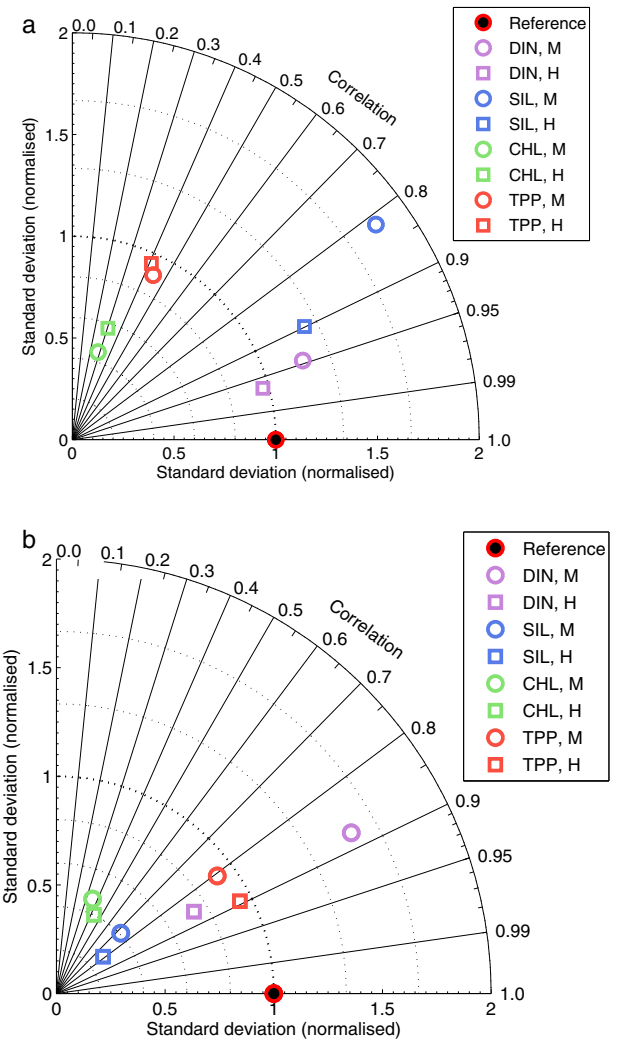

Figure 5. Following on from Figure 4, Taylor diagrams showing medium (M) and high (H)-resolution NEMO performance for annual average fields of surface dissolved inorganic nitrogen (DIN), surface silicic acid (SIL), surface chlorophyll (CHL), and vertically integrated primary production (TPP). The upper diagram shows the performance for the global domain, while the lower diagram shows the same for the combined study areas shown in Figure 12. Average period is 2000–2009.

deviations from observed geographical patterns discussed above. Similarly, vertically integrated primary production shows the same biases between the models, but the high-resolution instance shows improved performance in the North Atlantic, as well as elevated gyre productivity driven by mesoscale eddy activity.

By way of a summary, Figure 5 compares the same fields for both model instances and shows the results via two Taylor diagrams [*Taylor*, 2001]. The first of these considers the global domain, while the second focuses on the combined subpolar and polar regions shown in Figure 12 (see later). The coloring and symbols, respectively, denote different model properties and resolutions, and performance increases toward the red circle located at position 1 on the *x* axis (i.e., where correlation is perfect and normalized standard deviation matches that of the observations). At the global scale, the first diagram shows that both model instances perform best in terms of nutrients, particularly nitrogen, and worse for the other properties, particularly chlorophyll. This pattern is common across other models (see *Yool et al*. [2013a, 2013b], for a comparison with CMIP5 models). The diagram also shows that high-resolution MEDUSA generally performs better than medium resolution MEDUSA for these observational targets, though not universally. Meanwhile, in the case of the more restricted subpolar and polar regions, model performance changes, with nutrient fields represented less well (especially silicic acid), and biological fields slightly improved (especially production). In part, this improvement in biological fields is a function of lower values in this region, especially in the ice-bound Arctic where both the real and modeled system have limited activity. Comparing between the model instances again finds that high-resolution MEDUSA performs better, if only slightly, across the different properties.

As already noted above, MEDUSA has previously been validated at medium resolution, and its performance agrees additionally well with that of comparable CMIP5 models [*Yool et al*., 2013a]. It has also performed favorably in model intercomparison exercises at both Arctic [*Popova et al*., 2012] and global scales [*Kwiatkowski et al*., 2014]. Aspects of its biological performance at high resolution in the Arctic are examined in *Popova et al*. [2010], *Popova et al*. [2012], and Lawrence et al. (submitted manuscript, 2015).

3. Results and Discussion

As previously reported for medium resolution in *Yool et al*. [2013b], NEMO-MEDUSA experiences significant, global-scale change during 2000–2099 under the RCP 8.5 scenario. At high resolution (Table 1), surface

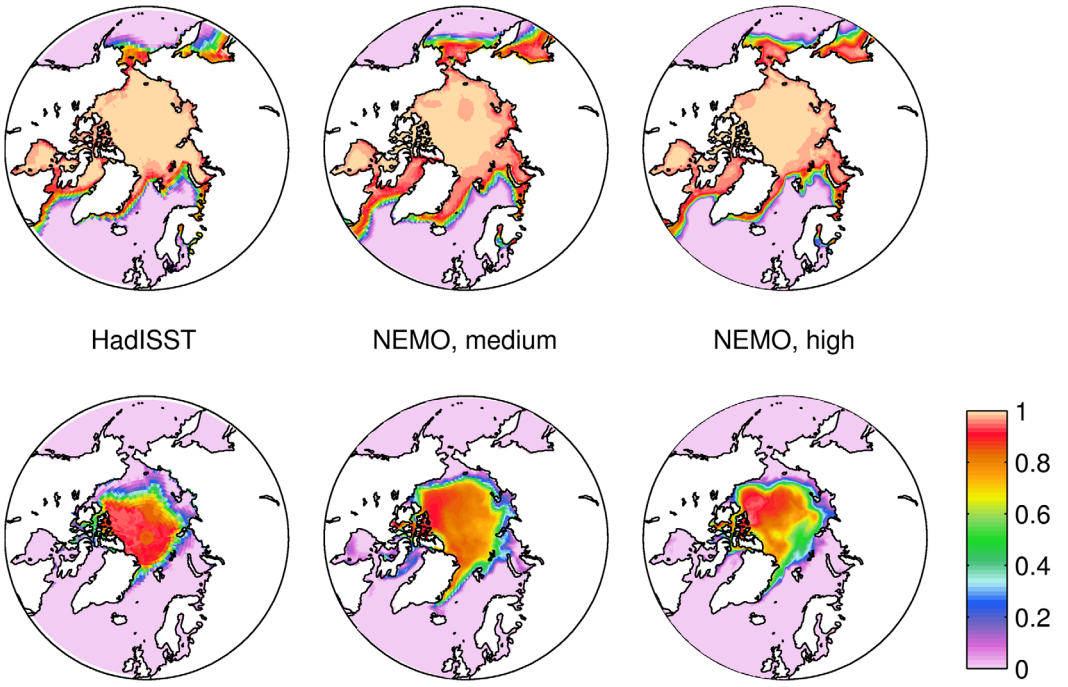

Figure 6. Average sea-ice concentration for (top) March (seasonal maximum) and (bottom) September (seasonal minimum) from (left) observations (HadISST), (middle) medium resolution NEMO, and (right) high-resolution NEMO. Average period is 2000–2009.

ocean warming of +3.3°C is accompanied by shoaling of the surface mixed layer by −22.8 m and by a decline in the extent of permanent sea-ice (= seasonal maximum) of more than 50% (14.0 → 6.9 × 10^6 km^2). In terms of biogeochemistry (Table 2), changes in surface DIN (−14.7%) and surface chlorophyll (−11.0%) are concurrent with a marked decline in global ocean productivity across the century from 45.8 to 42.8 Pg C yr^{-1} (−6.6%). However, as already remarked, change is not uniform across the World Ocean, and the Arctic, in particular, has experienced faster changes than other regions [*Serreze and Barry*, 2011], hence the focus of this study.

Table 1. Regional (Global, North Atlantic, North Pacific, and Arctic; Per Figure 12) Summaries of Decadal (2000s, 2050s, and 2090s) Values of Sea Surface Temperature (°C), Mixed Layer Depth (m), and Sea-Ice Extent (10^6 km^2) for High-Resolution NEMO[a]

	Global	North Atlantic	North Pacific	Arctic
Annual Mean Sea Surface Temperature				
2000s	18.43	9.17	6.53	−0.89
2050s	19.95	10.09	9.24	0.34
2090s	21.70	12.55	12.22	3.21
Annual Maximum Mixed Layer Depth				
2000s	110.0	317.9	106.4	67.7
2050s	90.8	104.2	98.5	88.9
2090s	87.2	82.4	92.7	89.9
Seasonal Maximum Mean Sea-Ice Area				
2000s	14.05	0.22	0.56	5.34
2050s	11.43	0.09	0.04	4.80
2090s	6.87	0.00	0.00	2.77
Seasonal Minimum Mean Sea-Ice Area				
2000s	4.67			3.58
2050s	0.20			0.12
2090s	0.00			0.00

[a]Seasonal maximum sea-ice is in March, while seasonal minimum is in September. Note that "global" sea-ice areas refer to Northern Hemisphere sea-ice only.

3.1. Arctic Change

Figure 7 illustrates the most dramatic change in the Arctic during the 21st century—the precipitous decline in sea-ice. The areas of March maximum and September minimum sea-ice extent are shown for both high and medium resolution NEMO. In terms of maximum extent, sea-ice in high-resolution NEMO declines gradually (though at a slowly increasing rate) from approximately 14 × 10^6 km^2 in the 2000s to around 8 × 10^6 km^2 by the early 2090s. However, from the mid-2090s, a rapid loss occurs, with the maximum extent dropping to almost 5 × 10^6 km^2 by 2099. The minimum extent remains relatively stable at around 5 × 10^6 km^2 through to the 2020s, before steadily declining until the 2050s, at which point minimum sea-ice extent rapid declines to near zero. While the two instances of

Table 2. Regional (Global, North Atlantic, North Pacific, and Arctic; Per Figure 12) Summaries of Decadal (2000s, 2050s, and 2090s) Values of Mean Annual Surface DIN (mmol N m^{-3}), Surface Chlorophyll (mg chl m^{-3}), and Vertically Integrated Primary Production (g C m^{-2} d^{-1}) for High-Resolution NEMO

	Global	North Atlantic	North Pacific	Arctic
Annual Mean Surface DIN				
2000s	4.98	4.61	9.99	4.10
2050s	4.67	2.25	7.84	3.01
2090s	4.25	1.16	5.30	2.17
Annual Mean Surface Chlorophyll				
2000s	0.254	0.523	0.540	0.265
2050s	0.240	0.416	0.551	0.217
2090s	0.226	0.307	0.530	0.194
Annual Mean Primary Production				
2000s	0.353	0.463	0.482	0.098
2050s	0.343	0.380	0.518	0.141
2090s	0.330	0.298	0.531	0.166

NEMO show similar patterns, both in terms of overall fate of sea-ice and interannual variability (due to their shared surface forcing), medium resolution NEMO consistently has more sea-ice than high-resolution NEMO. Minimum sea-ice extents begin the century around 1–1.5 $\times$ 10^6 km^2 apart, with maximum extents separated by around 1.5 $\times$ 10^6 km^2, but these gaps narrow during the century. This reduced ice cover at higher resolution is consistent with other findings that point to better resolution allowing smaller, warmer hydrographic features to be resolved [*Mahlstein and Knutti*, 2011]. Supporting information Figures S1 and S2 augment Figure 7 by presenting full monthly sea-ice extents for high and medium resolution NEMO respectively. Note that, in the case of medium resolution NEMO, the phenology of the seasonal sea-ice maximum shifts to April by the last decade of the 21st century.

Figures 8–10 show the time evolution of a series of key indicators and factors that regulate total ocean productivity, shown in Figure 11, for high-resolution NEMO (supporting information Figures S3–S6 show the corresponding properties for medium resolution NEMO). The projection used has been chosen to focus on the northern North Atlantic and the "Atlantic sector" of the Arctic Ocean.

Illustrating the most significant regional change, Figure 8 shows the change in the sea-ice concentration at its seasonal minimum extent for three decadal average periods: the 2000s, 2050s, and 2090s. In the 2000s, sea-ice covers most of this sector of the Arctic, albeit with large leads east of Greenland and north of the Barents Sea. As additionally indicated in this panel, the seasonal maximum extent (>15%) reaches further into the Barents Sea and Baffin Bay. However, by the 2050s, only a small remnant of this cover remains as low concentration ice floes on the north coast of Greenland. And by the 2090s, the extreme polar warming under RCP 8.5 means that no sea-ice persists to September in this sector of the Arctic at all. Although the maximum sea-ice extent remains large throughout the 21st century, it is clear from the 2090s panel that seasonal sea-ice growth in the winter significantly declines by the end of the century, with a significant "gap" northeast of the Franz Josef Land archipelago.

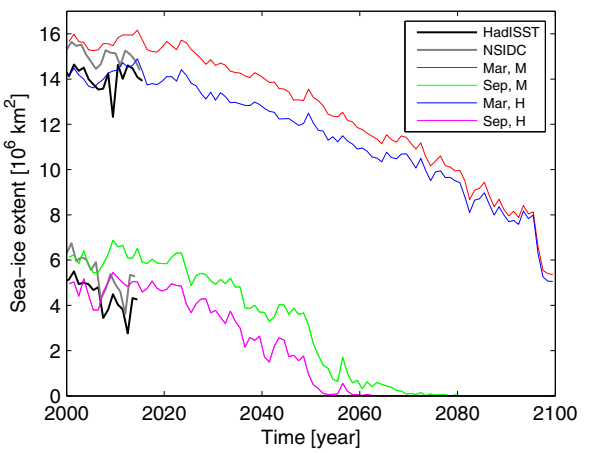

Figure 7. Observed and modeled maximum (March) and minimum (September) sea-ice extent for the 21st century. Observed extents shown for the HadISST (black) and NSIDC (grey) analyses. Modeled extents shown for both medium (M) and high (H)-resolution NEMO.

Figure 9 shows a further significant change in the physical conditions of this region, that of decadally averaged annual maximum mixed layer depth (MLD; defined by σ_T) for the same three decades. In the least anthropogenically perturbed state, the 2000s, maximum MLDs are greater than 1000 m, and are outside, but immediately adjacent to, the seasonal maximum sea-ice extent, principally the Labrador and Greenland-Iceland-Norwegian (GIN) seas. Through the 21st century, maximum MLD broadly tracks the poleward retreat in seasonal maximum sea-ice extent, moving ultimately to the north of the Barents Sea by the 2090s. Maximum MLD also significantly declines, both in terms of the size of the area experiencing deep convection and the depth to which mixing occurs. Overall,

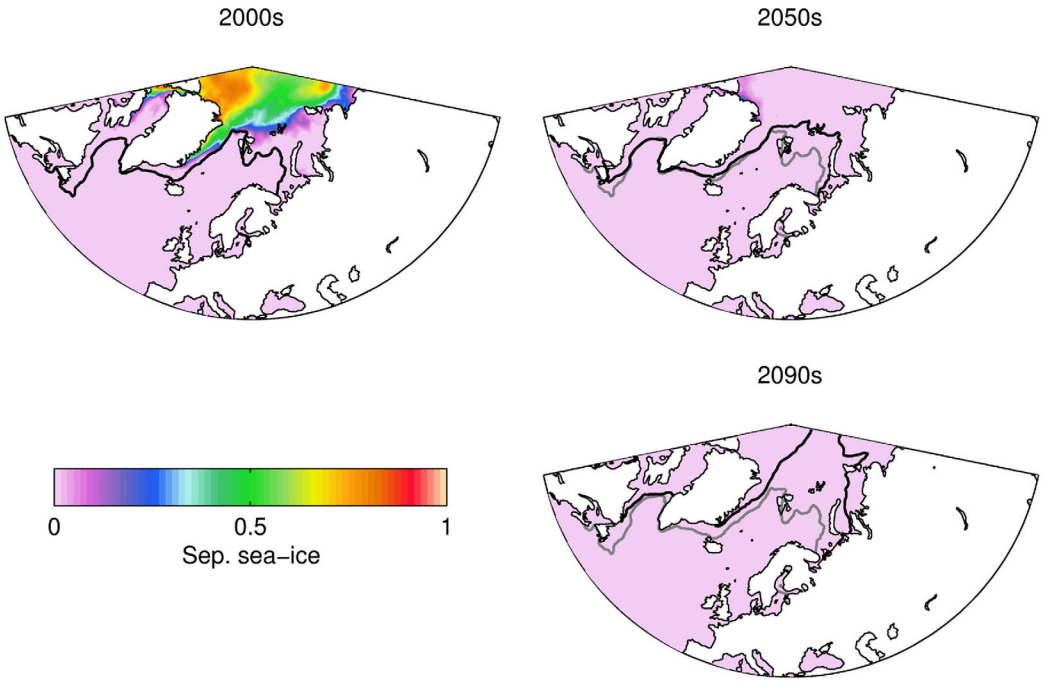

Figure 8. Decadally averaged sea-ice concentration at the annual minimum (September) in high-resolution NEMO for the 2000s, 2050s, and 2090s. The black lines on each figure show the corresponding 15% contour of sea-ice concentration at the annual maximum (March), with the additional grey lines marking this for the 2000s for comparison. Sea-ice concentration is nondimensional.

regions in the North Atlantic with deep maximum MLDs at the start of the 21st century experience strong shoaling (1000 m → 100 m), while maximum MLDs deepen slightly in the Arctic (50 m → 200 m) in parallel with sea-ice retreat. These marked changes in North Atlantic and Arctic MLD under climate change are consistent with findings with other models [*Capotondi et al.*, 2012].

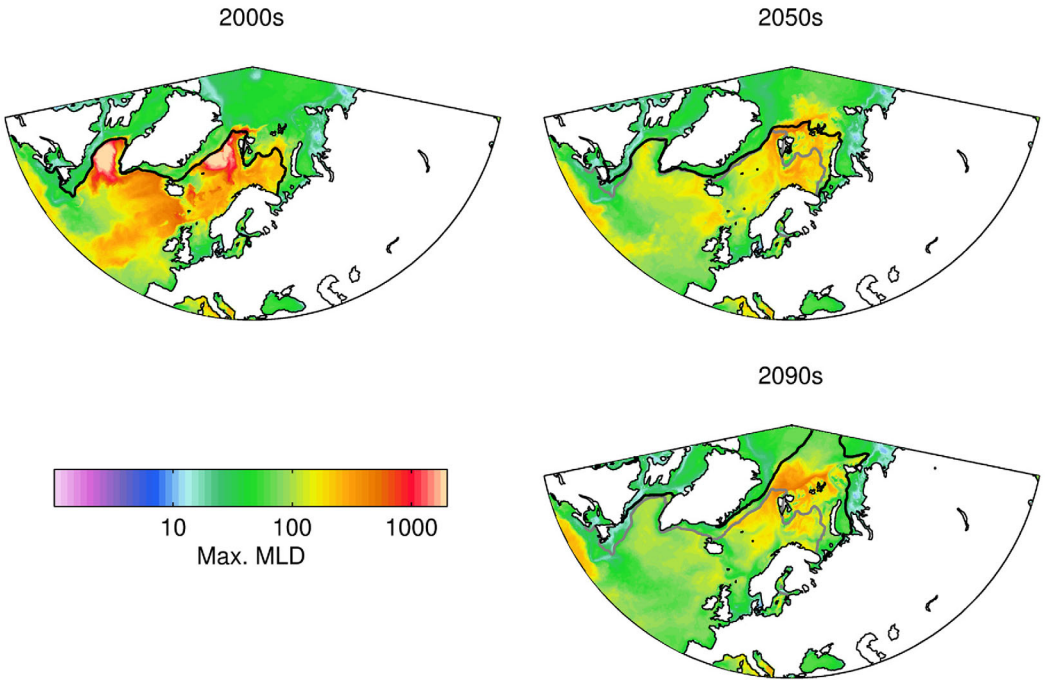

Figure 9. Decadally averaged annual maximum mixed layer depth in high-resolution NEMO for the 2000s, 2050s, and 2090s. The black lines on each figure show the 15% contour of sea-ice concentration at the annual maximum (March), with the additional grey lines marking this for the 2000s for comparison. Mixed layer depth is in m and is shown here on a logarithmic scale.

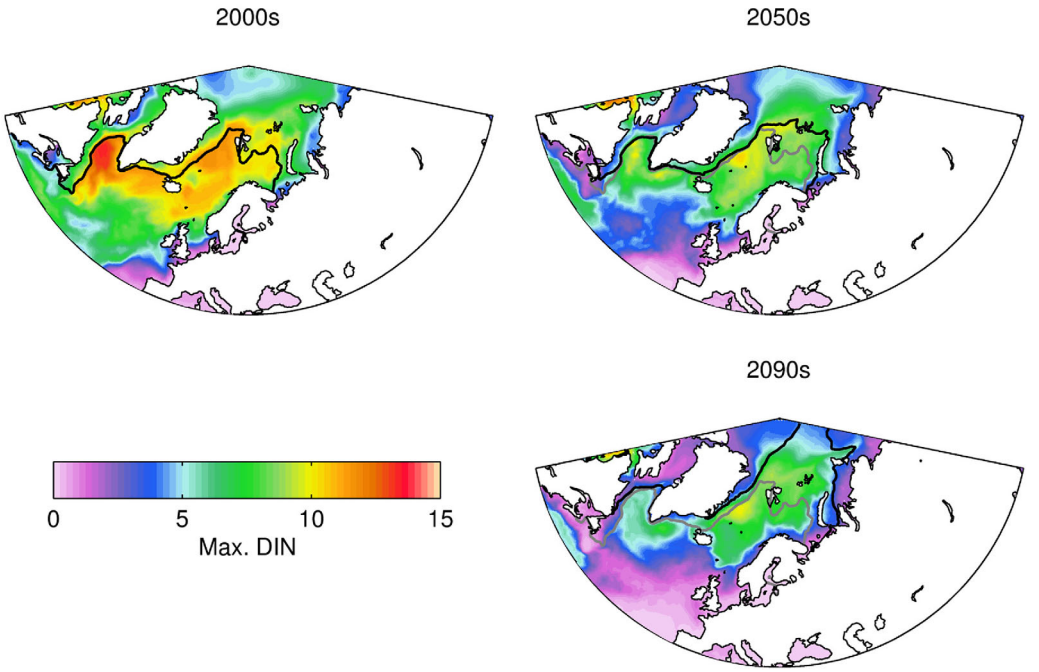

Figure 10. Decadally averaged annual maximum surface DIN in high-resolution NEMO for the 2000s, 2050s, and 2090s. The black lines on each figure show the 15% contour of sea-ice concentration at the annual maximum (March), with the additional grey lines marking this for the 2000s for comparison. Surface DIN is in mmol N m^{-3}.

A key impact of these changes in MLD can be seen in the patterns of seasonal maximum DIN shown in Figure 10. In the deep mixing regime of the Labrador Sea, the seasonal maximum of DIN halves across the 21st century (14 → 7 mmol m^{-3}), while in the GIN sea surface, DIN declines less precipitously (12 → 8 mmol m^{-3}). In

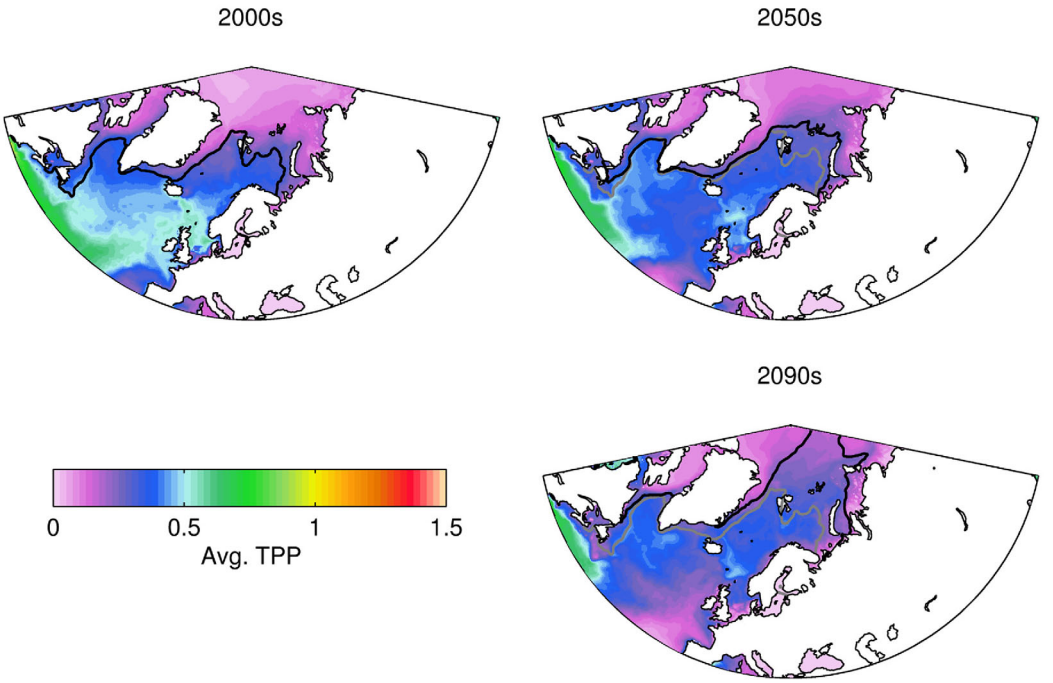

Figure 11. Decadally averaged vertically integrated primary production in high-resolution NEMO for the 2000s, 2050s, and 2090s. The black lines on each figure show the 15% contour of sea-ice concentration at the annual maximum (March), with the additional grey lines marking this for the 2000s for comparison. Vertically integrated primary production is in g C m^{-2} d^{-1}.

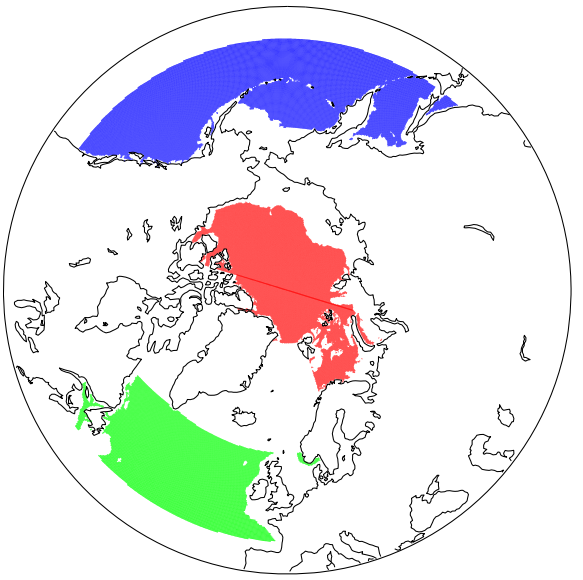

Figure 12. "Atlantic" (green), "Pacific" (blue), and "Arctic" (red) subregions used in this analysis. Atlantic and Pacific regions span 45°N–60°N, while the Arctic region spans 70°N–90°N. The Arctic region is modified to remove the "Atlantic Gateway" from the east coast of Greenland to the Barents Sea (17°E). All regions exclude shelf areas where the water column depth is less than 200 m. Note that, for simplicity, the subregions contain small areas—such as the Gulf of St. Lawrence, the Novaya Zemlya Trough, and residual sections of the North and Japan Seas—in which conditions may not be representative of the wider subregion.

the Arctic, nutrient concentrations decline slightly, despite increasing maximum MLD that might otherwise be expected to increase DIN concentrations. This change reflects both the preexisting vertical profiles of nutrients, as well as their removal through increased biological production made possible by the elevated submarine light driven, ultimately, by sea-ice decline. However, DIN concentrations also strongly decline toward limiting concentrations (<1 mmol m^{-3}) around North Atlantic and Arctic coasts, as well as in the deep, central Atlantic.

Reflecting this, Figure 11 shows decadally averaged vertically integrated primary production for the same three time slices. Change here is most pronounced across the deep, central Atlantic, where production falls by almost half across the 21st century (0.5 $\rightarrow$ 0.25 g C m^{-2} d^{-1}). In spite of large changes in mixing and surface DIN, change is much less significant in regions such as the Labrador and GIN seas, where production actually slightly increases because of improved growing conditions (better light conditions and warmer temperatures). In the Arctic, productivity rises everywhere throughout the region, although without approaching the levels found in productive Atlantic waters to the south.

Table 1 summarizes the changes in key physical characteristics for the same time periods for the North Atlantic and Arctic, and includes corresponding global averages (and those for the North Pacific; see later) for comparison. In terms of surface temperature change, the Arctic experiences a larger change (+4.1°C) than either the North Atlantic (+3.4°C) or global ocean (+3.3°C)—though markedly less than that simulated in the North Pacific (+5.7°C). Mixed layer depth shoals in the North Atlantic (−235 m), North Pacific (−14 m), and at the global scale (−23 m), but deepens in the Arctic (+22 m) in response to increased exposure to atmospheric forcing and a weakening halocline [cf. *Martinson and Steele*, 2001]. As noted already, sea-ice cover declines, with the seasonal maximum extent halving, and permanent ice cover (i.e., denoted by the seasonal minimum) disappearing entirely.

As supporting information Figures S3–S6 and Table S1 show, these patterns are repeated across model resolutions, although with some differences. Medium resolution NEMO generally has slightly more sea-ice across the whole of the 21st century, although experiences the same complete loss as high-resolution NEMO by the 2090s. Maximum mixed layer depths behave in a similar manner between resolutions, though the horizontal patterns differ somewhat because medium resolution NEMO has less focused regions of deep convection, and its Arctic mixing is generally shallower while sea-ice is present. These patterns are also reflected in maximum surface DIN distributions, although in medium resolution NEMO surface DIN concentrations are typically lower across this region. Productivity between model resolutions is again similar, with both NEMO instances showing large declines in the North Atlantic and moderate rises in the Arctic. But as with MLDs and surface DIN, the precise geographical details differ, primarily because of resolution-driven differences in physical hydrography.

3.2. Controls on Productivity

The consequences for ocean productivity of these changes in the physical and biogeochemical backgrounds of the North Atlantic and Arctic are investigated through a series of regional analyses. Figure 12 shows the delineation of the polar and subpolar ocean areas of the Northern Hemisphere into "Atlantic,"

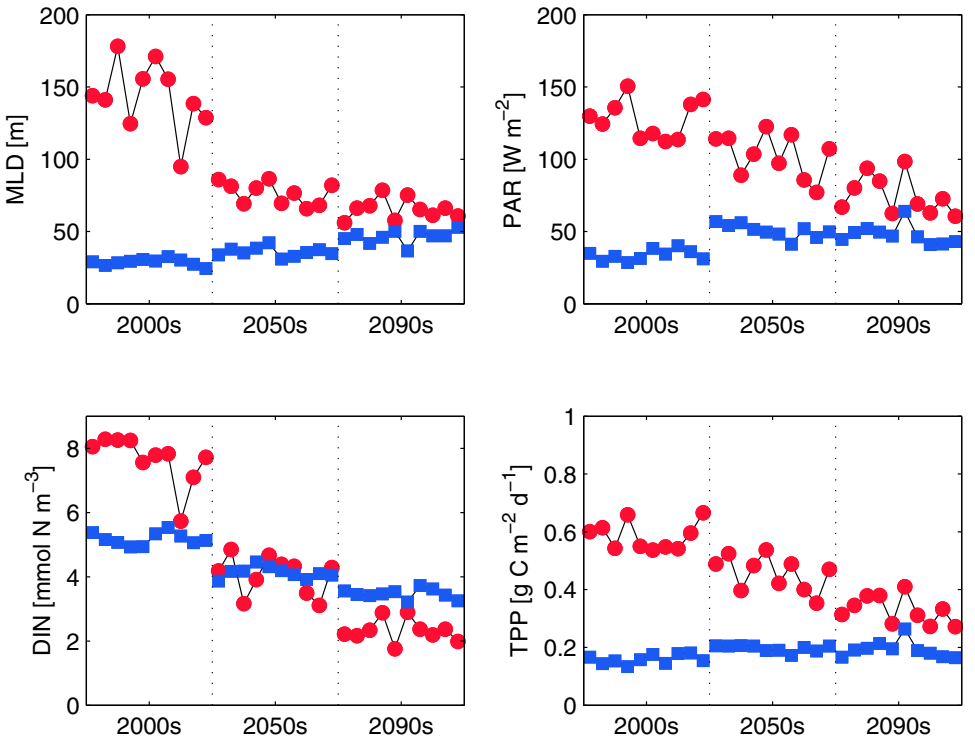

Figure 13. The time evolution for the 2000s, 2050s, and 2090s of (top left) prebloom MLD (m), (top right) surface PAR (W m^{-2}), (bottom left) surface DIN (mmol N m^{-3}), and (bottom right) vertically integrated TPP (g C m^{-2} d^{-1}) averaged across the North Atlantic (red) and Arctic Ocean (blue) for high-resolution NEMO.

"Pacific" (both 45°N–60°N), and Arctic (70°N–90°N) subregions. These are further constrained to deep water regions (>200 m depth), and by the exclusion of confounding peripheral areas such as the Baltic, Labrador, and Mediterranean Seas and Baffin and Hudson Bays. The "Arctic" subregion is additionally modified to omit the "Atlantic Gateway" region from East Greenland to the western margin of the Barents Sea, since this region is more representative of the Atlantic Ocean, despite its latitude. The resulting three regions were devised to capture characteristic domains in which the changes across the 21st century are broadly similar. The "Pacific" subregion is included here for comparison with the "Atlantic" subregion (see later).

Figures 13 and 14 illustrate the regional average changes in key regulating factors, as well as primary production, across the 21st century for prebloom and bloom periods, respectively. "Prebloom" is defined here as the month preceding the annual maximum surface chlorophyll concentration, while "bloom" is the month in which this annual maximum occurs. Restricting analysis to these specific periods aims to sidestep the shorter, insolation-limited growing season of the Arctic and examining both subregions solely during their peak seasonal activity. Bloom timing is determined locally on a grid cell by grid cell basis to reflect variability driven by local factors such as mixing, hydrography and sea-ice cover. As before, the 21st century is represented by three decades spanning periods of limited (2000s), moderate (2050s), and extreme (2090s) climate change. Each decade is represented with individual years to provide an indication of the interannual variability of the regional averages.

In terms of MLD, and as already suggested by Figure 10, prebloom conditions in the Atlantic alter to a large degree. Between the 2000s and the 2090s, average MLDs for the region drop from around 150 m to only 60 m. Change in the Arctic is the reverse of this, with MLDs increasing steadily through the century from around 25 to 50 m.

These patterns are largely repeated for the prebloom availability of surface photosynthetically available radiation (PAR), though prebloom Arctic PAR saturates by the 2050s. The decline of prebloom PAR in the Atlantic reflects a shift in the timing of the bloom maximum earlier to in the year, and while a similar shift occurs in the Arctic, prebloom PAR instead increases in this region as a result of the most quantitatively important decline of sea-ice.

Average prebloom nutrient concentrations shift in the same direction in both the Atlantic and Arctic, with both experiencing declines across the 21st century. The decline is more marked in the Atlantic (8 → 2 mmol N

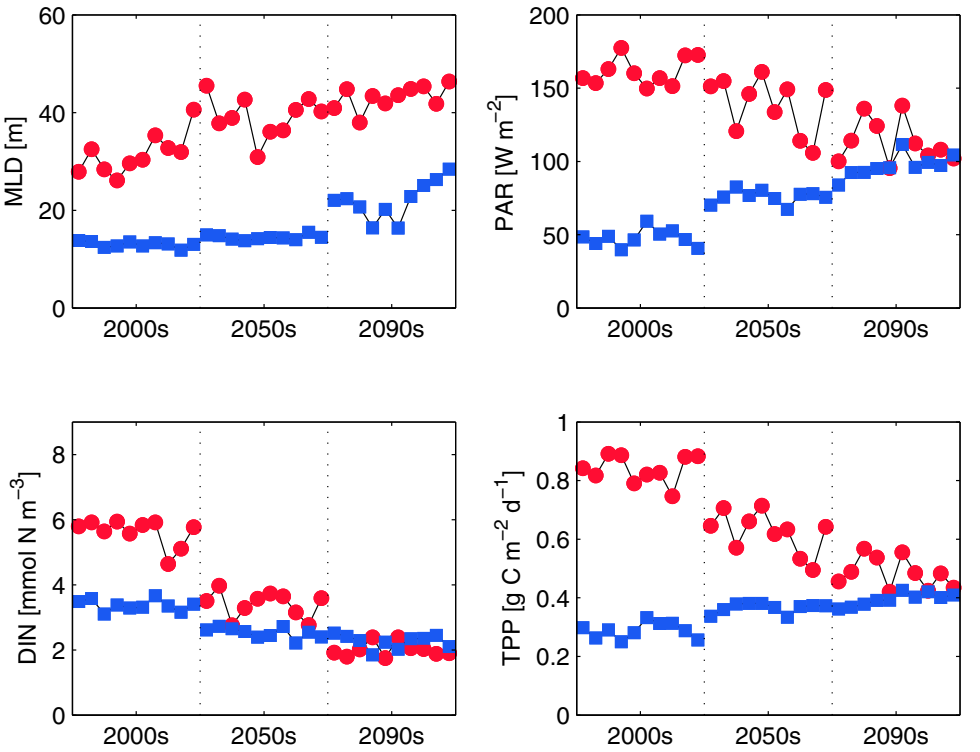

Figure 14. The time evolution for the 2000s, 2050s, and 2090s of bloom period (top left) MLD (m), (top right) surface PAR (W m^{-2}), (bottom left) surface DIN (mmol N m^{-3}), and (bottom right) vertically integrated TPP (g C m^{-2} d^{-1}) averaged across the North Atlantic (red) and Arctic Ocean (blue) for high-resolution NEMO.

m^{-3}) than the Arctic (6 → 3 mmol N m^{-3}), as it both starts higher and ends lower. However, in both subregions, prebloom concentrations remain above limiting concentrations (1 mmol N m^{-3}). Note that while Atlantic concentrations decline as would be expected with shoaling prebloom MLDs, Arctic concentrations instead decline despite an increase in the average prebloom mixing in this subregion. As Figure 15 shows, this decline of surface nutrient reflects the steadily deepening nutricline driven by increased Arctic productivity—concentrations that were normal for the surface ocean in the 2000s are only found below 100 m by the 2090s.

The changes in prebloom productivity are mixed between the subregions, with a marked decline across the 21st century in the Atlantic and marginally elevated production in the Arctic. In the Atlantic, this is in keeping with the corresponding declines in light and nutrients, although neither of these factors are at levels which fundamentally limit phytoplankton growth. In the Arctic, while DIN declines, PAR is rising, and the pattern of modest increases in primary production more closely tracks that of increased PAR availability than decreased DIN. This is perhaps unsurprising given that the prebloom Arctic, even by the end of the 21st century, is still not limited by DIN availability.

Switching to the situation at the bloom maximum, Figure 14 shows the corresponding comparisons between the Atlantic and Arctic. In terms of PAR, surface DIN, and primary production, the prebloom and bloom periods show the same regional patterns across the 21st century; however, mixed layer depth shows a different pattern in the Atlantic subregion. Here while prebloom period mixed layer depth declines significantly across the 21st century, bloom period mixed layer depth instead slightly increases from around 30 to 45 m. This may be caused by a shift in bloom timing, a shift in the seasonal cycle of mixing, or by changes in either (or both) due to shifts in spatial patterns. Deconvoluting the roles of these factors has not been examined here, though it may have implications for the dynamics of the Arctic's plankton ecosystem.

PAR is naturally higher in the bloom than prebloom period for both regions, but the shifting phenology of the bloom through the 21st century means that, in the Atlantic subregion, PAR becomes progressively lower at the time of the bloom. Much as in the prebloom period, in the Arctic subregion, the impact of sea-

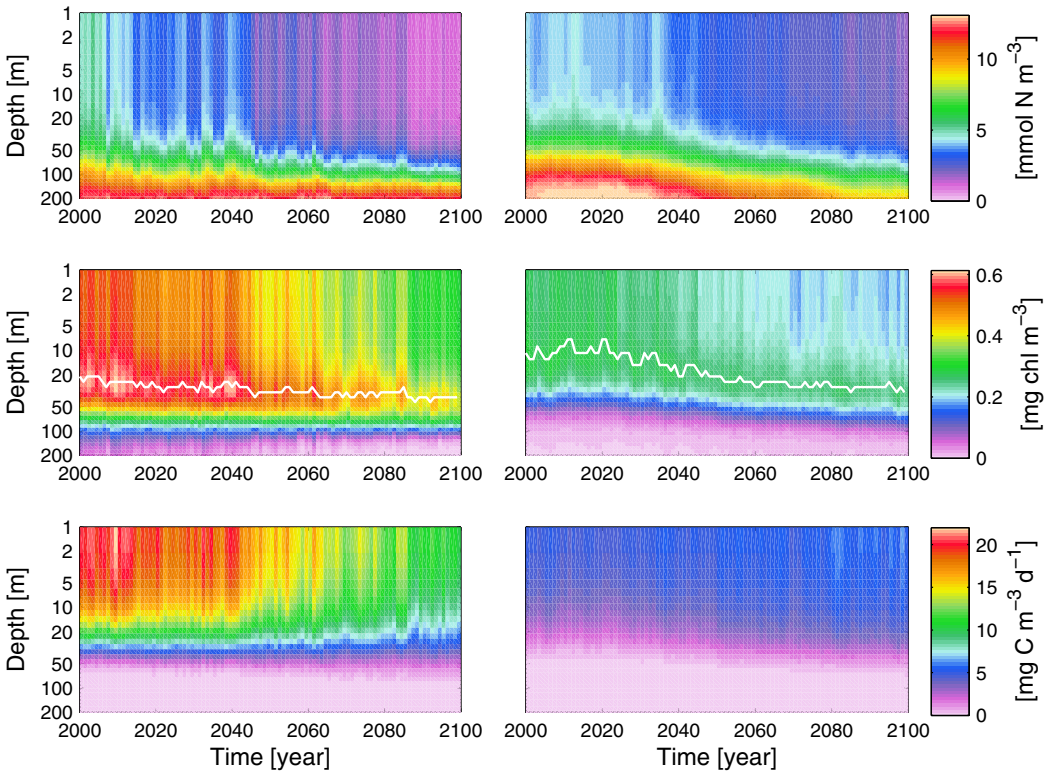

Figure 15. The time evolution of annually averaged vertical profiles of (top) DIN (mmol N m^{-3}), (middle) chlorophyll (mg chl m^{-3}), and (bottom) primary production (mg C m^{-3} d^{-1}) in the (left) North Atlantic and (right) Arctic for high-resolution NEMO. The white line shown in both plots of the middle row marks the depth of the deep chlorophyll maximum. Note that the vertical scale is logarithmic.

ice loss serves to elevate light across the 21st century for the blooms. Again, this occurs despite a shifting of bloom timing in the Arctic slightly earlier (though this is not universal; some locations now have later blooms).

The change in surface DIN across the 21st century shows almost the exact same patterns in prebloom and bloom periods for both subregions. In the Atlantic subregion, DIN concentrations drop from around 6 to 2 mmol N m^{-3} over the 21st century, driven by a loss of winter nutrient entrainment reflected in the mixed layer depth changes already discussed. The Arctic subregion shows a more modest decline, but by the end of the century peak bloom conditions are almost half of those at the start.

The time evolution of primary production in both subregions during the bloom period largely follows that in the prebloom period. In the Atlantic, productivity undergoes a significant drop (0.8–0.5 g C m^{-2} d^{-1}), in keeping with the correspondingly large fall in surface nutrient availability. Meanwhile, the Arctic exhibits a similar modest increase in bloom productivity. This is understandably elevated over that of the prebloom period, reaching area average values just below those of the Atlantic by the 2090s.

Overall, the geographically averaged patterns of controlling factors and productivity behave broadly consistently whether prebloom or bloom periods are considered. The Atlantic subregion is generally transitioning from productive conditions driven by deep winter mixing and nutrient replenishment to a state in which productivity is significantly reduced (−35.6%). Somewhat in contrast, the Arctic is being driven from conditions of light limited, low productivity to those in which sea-ice is seasonally absent and light limitation is much less important. Nonetheless, Arctic subregion productivity (0.17 g C m^{-2} d^{-1}) remains considerably lower than that of the Atlantic at its peak (0.46 g Cm^{-2} d^{-1}; Table 2).

Finally, supporting information Figures S9 and S10 show corresponding results from medium resolution NEMO. While there are some differences—for instance, elevated 2050s nutrients in the Arctic—the patterns of response are consistent between both instances of NEMO.

3.3. Synthesis and Context

The preceding results illustrate a clear pattern of biogeochemical change in the Atlantic and Arctic that is rooted in physical change in the ocean. Principally, increased stratification (driven thermally and, in the Arctic, also by freshening) shoals turbulent mixing and leads to a decline in the resupply of nutrients to the upper ocean. In the Atlantic, this translates to a straightforward, if extreme, decline of biological productivity. In the Arctic, this decline is offset by the concomitant increase in the general availability of light in this region. However, biogeochemical parallels can be drawn across both regions.

Figure 15 shows regionally averaged vertical profiles of DIN, chlorophyll, and productivity for the Atlantic and Arctic subregions of high-resolution NEMO (supporting information Figure S11 shows the corresponding profiles for medium resolution NEMO). Consistent with the changes at the surface, DIN concentrations in the upper 100 m decline throughout the 21st century in both subregions, with the change in the Atlantic (starting higher and finishing lower) particularly pronounced. This pattern is imprinted on the chlorophyll time series, which shows declining surface concentrations in both regions in parallel with a deepening of the chlorophyll maximum (indicated by a white line). Productivity, however, shows differences between the regions. In the Atlantic, it declines throughout the century, but remains highest (on an annual average basis) in the upper ocean, and does not track the descending deep chlorophyll maximum. Meanwhile, in the Arctic, productivity increases—gradually and slightly—across the century, with increases at depth and at the surface, despite these changes in DIN.

Figure 16 presents an integration of the changes in nutrient status and in productivity for both the Atlantic and Arctic subregions, and for both model resolutions. With key years highlighted (2000, 2050, and 2099), the figure shows the trajectories of model travel in both subregions for productivity and integrated (0–100 m) DIN. The Atlantic story is well known, and sees the model decline from high nutrients and high productivity to much lower values of both. By virtue of permanent sea-ice cover in early 21st century, the Arctic starts with low productivity (despite similarly high nutrients), but this gradually increases in parallel with a decline in nutrients as climate change impact grows. By the end of the 21st century, the Atlantic and Arctic have almost converged, both in terms of nutrients and productivity, and have done so toward a state (200 mmol N m^{-3}, 0.2 g C m^{-2} d^{-1}) that is close to that which typically occurs at the periphery of the subtropical gyres. While the details differ slightly between model resolutions—for instance, at medium resolution, the Arctic dawdles in the first half of the 21st century before sprinting in the second half—the patterns are closely repeated.

For wider context, supporting information Figure S12 places the change in the Atlantic subregion alongside that in the Pacific subregion and the World Ocean as a whole. The Pacific does not see change in productivity like that in the Atlantic, primarily because higher integrated nutrients place it further away from the "cliff edge" of productivity decline. Instead, productivity actually increases in both model runs, primarily a response to warmer temperatures and faster biological rates [*Yool et al.*, 2013b]. That said, despite a shared productivity response, the medium and high-resolution models disagree on the future of this region. The medium resolution model suggests a future in which nutrients are largely unchanged (i.e., years 2000, 2050, and 2099 line up vertically), but the high-resolution model instead sees a steady decline in nutrient stocks. Ultimately this may lead to a collapse in productivity in the Pacific that parallels that in the Atlantic. However, with respect to the preceding Atlantic-Arctic comparison, it also points to model resolution playing a role that, region to region, can vary in importance.

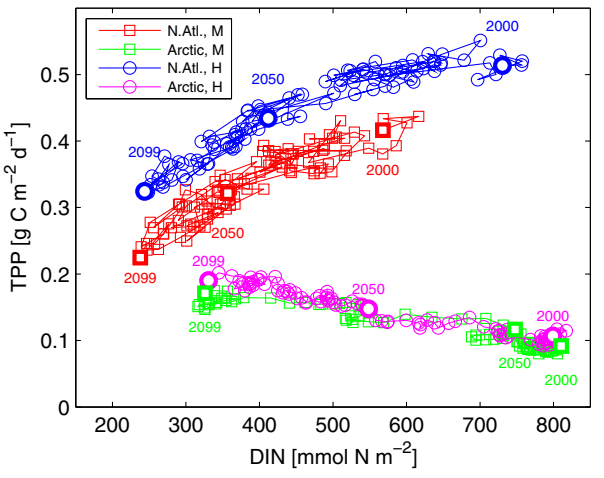

Figure 16. The time evolution of vertically integrated DIN (0–100 m; mmol N m^{-2}) against vertically integrated primary production (0–100 m; g C m^{-2} d^{-1}) for the North Atlantic (medium, red; high, blue) and Arctic (medium, green; high, magenta) in both high and medium resolution NEMO.

On a related note, although the model resolutions used here clearly (and

inevitably) differ in their representation of surface currents and ocean circulation (cf. Figure 3), it is still the case that much of the modeled biogeochemistry (i.e., magnitudes and distributions) remains very similar. The details of model features can clearly be seen to be different, but in crude, bulk terms, this work tends to suggest that increased resolution does not give transformatively different results in the Arctic, at least for NEMO-MEDUSA. This is not an argument against resolution (and computational cost) increases in ocean modeling (cf. section 2.4's validation), but does suggest that current forecasts of the future Arctic may be unlikely to change drastically as resolution improves. Instead, narrowing the range of the disparate behavior of Arctic biogeochemistry in current generation models found by *Popova et al*. [2012] and *Vancoppenolle et al*. [2013] will arguably be of greater importance (see below). All that said, where specific physical features such as currents or upwelling are key factors in local ecosystems (or for local communities), representing these well, and modeling their change well, will still be important.

Although much of the discussion above focuses on differences between the medium and high-resolution instances, both are essentially in agreement on increasing Arctic productivity throughout the 21st century (per Figure 16). As briefly mentioned above, in their synthesis of 21st century projections by CMIP5 models, *Vancoppenolle et al*. [2013] found that a range of futures are simulated, including some where Arctic productivity is actually lower by the end of the century. This diversity was foreshadowed by an earlier model intercomparison of the "present-day" Arctic by *Popova et al*. [2012], which found that the current sea-ice regime regulated primary production largely through light limitation rather than the availability of nutrients. This meant that models could agree on current productivity while having quite different patterns of nutrient distribution, with the potential for disparate behavior under an ice-free future, much as *Vancoppenolle et al*. [2013] subsequently found. Consequently, the analysis here is necessarily limited to a particular future, and its results cannot reflect the current range of forecasts for the future Arctic. However, in this context, and as noted in section 2.4, and previously by *Popova et al*. [2012], MEDUSA's performance in the current Arctic is broadly consistent with observations.

Notwithstanding the above, this study has a number of associated caveats. As already noted, analysis has focused on a single model, NEMO-MEDUSA, and a single future scenario, RCP 8.5, although it has done so for two resolutions of the model. As with all models, NEMO-MEDUSA has a number of deficiencies in its representation of the ocean, some of which manifest in the validation earlier [see also *Yool et al*., 2013a]. Additionally, NEMO-MEDUSA includes a number of assumptions that, under strong future climate change, result in marked shifts in its behavior (e.g., strong ocean acidification feedbacks) [*Yool et al*., 2013b; *Popova et al*., 2014]. More broadly, the use of atmospheric forcing rather than a coupled atmosphere prevents NEMO-MEDUSA from including certain ocean-atmosphere interactions, although in the specific case here, it allows both model resolutions to experience identical surface forcing.

4. Conclusions

1. During the 21st century, mean global productivity is projected to decline from 45.8 to 42.8 Pg C yr^{-1} (-6.6%) in high-resolution NEMO.
2. This modest drop globally is offset by large regional changes: in the subpolar North Atlantic, productivity falls by -35.7%, while in the Arctic, productivity instead increases by $+69.8\%$.
3. In the North Atlantic, climate change-driven stratification translates into large changes in mixed layer depth (318 $\rightarrow$ 82 m), reduced deep water entrainment, and falling surface DIN concentrations (4.6 $\rightarrow$ 1.2 mmol N m^{-3}) which act to drive these productivity changes.
4. Meanwhile, in the Arctic, the complete loss of summertime sea-ice cover (4.7 $\rightarrow$ 0.0 $\times$ 106 km^2) significantly increases the availability of light for primary production.
5. These climate shifts drive a series of changes in both regions, some of which are common, some of which are in opposition, but the net effect of climate change is convergence in terms of bulk nutrients and productivity.
6. Consequently, the Arctic is not the "new Atlantic," and instead loses much of its unique (sea-ice driven) character to resemble the "future Atlantic."
7. While there are differences in projected changes between model resolutions, in particular at the scales of major current systems and subregional features, the picture at globally and regionally integrated scales remains the same.

Acknowledgments
The authors would like to acknowledge the role of the Forum for Arctic Modeling & Observational Synthesis (FAMOS), funded by the National Science Foundation Office of Polar Programs (awards PLR-1313614 and PLR-1203720). This has provided an invaluable focus for the Arctic community, and the authors are grateful to the organizers of FAMOS, its participants, and to the Editor of this Special Issue, Andrey Proshutinsky. The authors are particularly grateful for the detailed and helpful criticism and comments made by two anonymous referees on an earlier draft of this manuscript. By identifying omissions in content and analysis, as well as lapses in clarity, these referees greatly improved its revised final form. The authors would additionally like to acknowledge helpful comments provided by attendees at the North Pacific Marine Science Organization (PICES) Third International Symposium (Santos City, Brazil). The authors gratefully acknowledge the financial support of the Natural Environmental Research Council (NERC) and the European Union Seventh Framework Programme (FP7). The work was primarily supported by NERC National Capability funding and the Regional Ocean Modelling project (ROAM; grant NE/H017372/1), part of the NERC UK Ocean Acidification research programme (UKOA). Funding was also provided by the FP7 EURO-BASIN project (FP7/2007-2013 and ENV.2010.2.2.1-1; grant agreement 264933). The high-resolution component of this work used the ARCHER UK National Supercomputing Service (http://www.archer.ac.uk). The HadGEM2-ES atmospheric forcing was produced by the UKMO and made available for use in NEMO by Dan Bernie (UKMO). Work to perform HadGEM2-ES simulations was supported by the EU-FP7 COMBINE project (grant 226520). Model output used in the production of this work may be obtained by contacting A.Y. (axy@noc.ac.uk).

References

Ardyna, M., M. Babin, M. Gosselin, E. Devred, L. Rainville, and J.-É. Tremblay (2014), Recent Arctic Ocean sea ice loss triggers novel fall phytoplankton blooms, *Geophys. Res. Lett.*, *41*, 6207–6212, doi:10.1002/2014GL061047.

Armstrong, R. A., C. Lee, J. I. Hedges, S. Honjo, and S. G. Wakeham (2002), A new, mechanistic model for organic carbon fluxes in the ocean: Based on the quantitative association of POC with ballast minerals, *Deep Sea Res., Part II*, *49*, 219–236.

AVISO (2014), *SSALTO/DUACS User Handbook, (M)SLA and (M)ADT Near-Real Time and Delayed Time Products*, CLS-DOS-NT-06-034, SALP-MU-P-EA-21065-CLS, 59 pp., Cent. Natl. Etud. Spatiales, Paris, France. [Available at http://www.aviso.altimetry.fr/fileadmin/documents/data/tools/hdbk_duacs.pdf.]

Behrenfeld, M. J., and P. G. Falkowski (1997), Photosynthetic rates derived from satellite-based chlorophyll concentration, *Limnol. Oceanogr.*, *42*, 1–20.

Boss, E., and M. Behrenfeld (2010), In situ evaluation of the initiation of the North Atlantic phytoplankton bloom, *Geophys. Res. Lett.*, *37*, L18603, doi:10.1029/2010GL044174.

Capotondi, A., M. A. Alexander, N. A. Bond, E. N. Curchitser, and J. D. Scott (2012), Enhanced upper ocean stratification with climate change in the CMIP3 models, *J. Geophys. Res.*, *117*, C04031, doi:10.1029/2011JC007409.

Carr, M.-E., et al. (2006), A comparison of global estimates of marine primary production from ocean color, *Deep Sea Res., Part II*, *53*, 741–770.

Cole, H., S. Henson, A. Martin, and A. Yool (2012), Mind the gap: The impact of missing data on the calculation of phytoplankton phenology metrics, *J. Geophys. Res.*, *117*, C08030, doi:10.1029/2012JC008249.

Dagg, M. J., and J. T. Turner (1982), The impact of copepod grazing on the phytoplankton of Georges Bank and the New York Bight, *Can. J. Fish. Aquat. Sci.*, *39*, 979–990, doi:10.1139/f82-133.

DRAKKAR Group (2007), Eddy-permitting Ocean Circulation Hindcasts of past decades, *CLIVAR Exch.*, *42*(12), 8–10.

Dunne, J. P., J. L. Sarmiento, and A. Gnanadesikan (2007), A synthesis of global particle export from the surface ocean and cycling through the ocean interior and on the seafloor, *Global Biogeochem. Cycles*, *21*, GB4006, doi:10.1029/2006GB002907.

DuRand, M. D., R. J. Olson, and S. W. Chisholm (2001), Phytoplankton population dynamics at the Bermuda Atlantic Time-series station in the Sargasso Sea, *Deep Sea Res., Part II*, *48*, 1983–2003, doi:10.1016/S0967-0645(00)00166-1.

Dutkiewicz, S., M. J. Follows, and P. Parekh (2005), Interactions of the iron and phosphorus cycles: A three-dimensional model study, *Global Biogeochem. Cycles*, *19*, GB1021, doi:10.1029/2004GB002342.

Fichefet, T., and M. A. Morales Maqueda (1997), Sensitivity of a global sea ice model to the treatment of ice thermodynamics and dynamics, *J. Geophys. Res.*, *102*, 12,609–12,646.

Findlay, H. S., A. Yool, M. Nodale, and J. W. Pitchford (2006), Modelling of autumn plankton bloom dynamics, *J. Plankton Res.*, *28*, 209–220, doi:10.1093/plankt/fbi114.

Flato, G., et al. (2013), Evaluation of climate models, in *Climate Change 2013: The Physical Science Basis, Contribution of Working Group I to the Fifth Assessment Report of the Intergovernmental Panel on Climate Change*, edited by T. F. Stocker et al., pp. 741–866, Cambridge Univ. Press, Cambridge, U. K., doi:10.1017/CBO9781107415324.020.

Garcia, H. E., R. A. Locarnini, T. P. Boyer, J. I. Antonov, O. K. Baranova, M. M. Zweng, and D. R. Johnson (2010a), *World Ocean Atlas 2009, vol. 3, Dissolved Oxygen, Apparent Oxygen Utilization, and Oxygen Saturation, NOAA Atlas NESDIS 70*, edited by S. Levitus, 344 pp., U.S. Gov. Print. Off., Washington, D. C.

Garcia, H. E., R. A. Locarnini, T. P. Boyer, J. I. Antonov, M. M. Zweng, O. K. Baranova, and D. R. Johnson (2010b), *World Ocean Atlas 2009, vol. 4, Nutrients (Phosphate, Nitrate, Silicate), NOAA Atlas NESDIS 71*, edited by S. Levitus, 398 pp., U.S. Gov. Print. Off., Washington, D. C.

Gaspar, P., Y. Grégoris, and J.-M. Lefevre (1990), A simple eddy kinetic energy model for simulations of the oceanic vertical mixing tests at station papa and long-term upper ocean study site, *J. Geophys. Res.*, *95*, 16,179–16,193.

Gran, H. H., and T. Braarud (1935), A quantitative study of the phytoplankton in the Bay of Fundy and the Gulf of Maine (including observations on hydrography, chemistry and turbidity), *J. Biol. Board Can.*, *1*, 279–467, doi:10.1139/f35-012.

Heinrich, A. K. (1962), The life histories of plankton animals and seasonal cycles of plankton communities in the oceans, *J. Cons. Int. Explor. Mer*, *27*, 15–25.

Hibler, W. D. (1979), A dynamic thermodynamic sea ice model, *J. Phys. Oceanogr.*, *9*, 815–846.

Hulburt, E. M., J. H. Ryther, and R. R. L. Guillard (1960), The phytoplankton of the Sargasso Sea off Bermuda, *J. Cons. Int. Explor. Mer*, *25*, 115–128.

Jones, C. D., et al. (2011), The HadGEM2-ES implementation of CMIP5 centennial simulations, *Geosci. Model Dev.*, *4*, 543–570, doi:10.5194/gmd-4-543-2011.

Key, R. M., A. Kozyr, C. L. Sabine, K. Lee, R. Wanninkhof, J. L. Bullister, R. A. Feely, F. J. Millero, C. Mordy, and T.-H. Peng (2004), A global ocean carbon climatology: Results from Global Data Analysis Project (GLODAP), *Global Biogeochem. Cycles*, *18*, GB4031, doi:10.1029/2004GB002247.

Klaas, C., and D. Archer (2002), Association of sinking organic matter with various types of mineral ballast in the deep sea: Implications for the rain ratio, *Global Biogeochem. Cycles*, *16*(4), 1116, doi:10.1029/2001GB001765.

Kwiatkowski, L., et al. (2014), iMarNet: An ocean biogeochemistry model inter-comparison project within a common physical ocean modelling framework, *Biogeosci. Discuss.*, *11*, 10,537–10,569, doi:10.5194/bgd-11-10537-2014.

Large, W. G., and S. G. Yeager (2009), The global climatology of an interannually varying air-sea flux data set, *Clim. Dyn.*, *33*, 341–364, doi:10.1007/s00382-008-0441-3.

Madec, G. (2008), *NEMO Reference Manual, Ocean Dynamic Component: NEMO–OPA, Note du Pole de Modélisation, Tech. Rep. 27*, Inst. Pierre Simmon Laplace, Paris.

Madec, G., P. Delecluse, M. Imbard, and C. Lévy (1998), *OPA 8.1 Ocean General Circulation Model Reference Manual, Note du Pole de Modélisation, Tech. Rep. 11*, 91 pp., Inst. Pierre Simon Laplace, Paris.

Mahlstein, I., and R. Knutti (2011), Ocean heat transport as a cause for model uncertainty in projected arctic warming, *J. Clim.*, *24*, 1451–1460, doi:10.1175/2010JCLI3713.1.

Martinson, D. B., and M. Steele (2001), Future of the Arctic sea ice cover: Implications of an Antarctic analog, *Geophys. Res. Lett.*, *28*, 307–310, doi:10.1029/2000GL011549.

Marzocchi, A., J. J.-M. Hirschi, N. P. Holliday, S. A. Cunningham, A. T. Blaker, and A. C. Coward (2015), The North Atlantic subpolar circulation in an eddy-resolving global ocean model, *J. Mar. Syst.*, *142*, 126–143.

Meier, W., F. Fetterer, M. Savoie, S. Mallory, R. Duerr, and J. Stroeve (2013), NOAA/NSIDC climate data record of passive microwave sea ice concentration, version 2, http://dx.doi.org/10.7265/N55M63M1, Natl. Snow Ice Data Cent., Boulder, Colo.

Mongin, M., D. M. Nelson, P. Pondaven, and P. Tréguer (2006), Simulation of upper–ocean biogeochemistry with a flexible–composition phytoplankton model: C, N and Si cycling and Fe limitation in the Southern Ocean, *Deep Sea Res., Part II*, *53*, 601–619.

Mundy, C. J., et al. (2009), Contribution of under-ice primary production to an ice-edge upwelling phytoplankton bloom in the Canadian Beaufort Sea, *Geophys. Res. Lett.*, *36*, L17601, doi:10.1029/2009GL038837.
O'Reilly, J. E., S. Maritorena, B. G. Mitchell, D. A. Siegal, K. L. Carder, S. A. Garver, M. Kahru, and C. McClain (1998), Ocean color chlorophyll algorithms for SeaWiFS, *J. Geophys. Res.*, *103*, 24,937–24,953.
Perrette, M., A. Yool, G. D. Quartly, and E. E. Popova (2011), Near-ubiquity of ice-edge blooms in the Arctic, *Biogeosciences*, *8*, 515–524, doi:10.5194/bg-8-515-2011.
Pingree, R. D., P. R. Pugh, P. M. Holligan, and G. R. Forster (1975), Summer phytoplankton blooms and red tides along tidal fronts in approaches to the English Channel, *Nature*, *258*, 672–677, doi:10.1038/258672a0.
Popova, E. E., A. Yool, A. C. Coward, Y. K. Aksenov, S. G. Alderson, B. A. de Cuevas, and T. R. Anderson (2010), Control of primary production in the Arctic by nutrients and light: Insights from a high resolution ocean general circulation model, *Biogeosciences*, *7*, 3569–3591, doi:10.5194/bg-7-3569-2010.
Popova, E. E., A. Yool, A. C. Coward, F. Dupont, C. Deal, S. Elliott, E. Hunke, M. Jin, M. Steele, and J. Zhang (2012), What controls primary production in the Arctic Ocean? Results from an intercomparison of five general circulation models with biogeochemistry, *J. Geophys. Res.*, *117*, C00D12, doi:10.1029/2011JC007112.
Popova, E. E., A. Yool, Y. Aksenov, A. C. Coward, and T. R. Anderson (2014), Regional variability of acidification in the Arctic: A sea of contrasts, *Biogeosciences*, *11*, 293–308, doi:10.5194/bg-11-293-2014.
Rayner, N. A., D. E. Parker, E. B. Horton, C. K. Folland, L. V. Alexander, D. P. Rowell, E. C. Kent, and A. Kaplan (2003), Global analyses of sea surface temperature, sea ice, and night marine air temperature since the late nineteenth century, *J. Geophys. Res.*, *108*(D14), 4407, doi:10.1029/2002JD002670.
Ridgwell, A., I. Zondervan, J. C. Hargreaves, J. Bijma, and T. M. Lenton (2007), Assessing the potential long-term increase of oceanic fossil fuel CO_2 uptake due to CO_2-calcification feedback, *Biogeosciences*, *4*, 481–492, doi:10.5194/bg-4-481-2007.
Riley, G. A. (1942), The relationship of vertical turbulence and spring diatom flowerings, *J. Mar. Res.*, *5*, 67–87.
Sakshaug, E., and H. R. Skjoldal (1989), Life at the ice edge, *Ambio*, *18*, 60–67.
Semtner, A. J. (1976), A model for the thermodynamic growth of sea ice in numerical investigation of climate, *J. Phys. Oceanogr.*, *6*, 376–389.
Serreze, M. C., and R. G. Barry (2011), Processes and impacts of Arctic amplification: A research synthesis, *Global Planet. Change*, *77*, 85–96, doi:10.1016/j.gloplacha.2011.03.004.
Serreze, M. C., M. M. Holland, and J. Stroeve (2007), Perspectives on the Arctic's shrinking sea-ice cover, *Science*, *315*, 1533–1536, doi:10.1126/science.1139426.
Siegel, D. A., S. C. Doney, and J. A. Yoder (2002), The North Atlantic spring phytoplankton bloom and Sverdrup's critical depth hypothesis, *Science*, *296*, 730–733, doi:10.1126/science.1069174.
Sverdrup, H. U. (1953), On conditions for the vernal blooming of phytoplankton, *J. Cons. Int. Explor. Mer*, *18*, 287–295.
Taylor, J. R., and R. Ferrari (2011), Shutdown of turbulent convection as a new criterion for the onset of spring phytoplankton blooms, *Limnol. Oceanogr. Methods*, *56*, 2293–2307, doi:10.4319/lo.2011.56.6.2293.
Taylor, K. E. (2001), Summarizing multiple aspects of model performance in a single diagram, *J. Geophys. Res.*, *106*, 7183–7192.
Timmermann, R., H. Goosse, G. Madec, T. Fichefet, C. Ethe, and V. Duliere (2005), On the representation of high latitude processes in the ORCA-LIM global coupled sea ice-ocean model, *Ocean Model.*, *8*, 175–201, doi:10.1016/j.ocemod.2003.12.009.
Townsend, D. W., M. D. Keller, M. E. Sieracki, and S. G. Ackleson (1992), Spring phytoplankton blooms in the absence of vertical water column stratification, *Nature*, *360*, 59–62.
Vancoppenolle, M., L. Bopp, G. Madec, J. Dunne, T. Ilyina, P. R. Halloran, and N. Steiner (2013), Future Arctic Ocean primary productivity from CMIP5 simulations: Uncertain outcome, but consistent mechanisms, *Global Biogeochem. Cycles*, *21*, GB4006, doi:10.1029/2006GB002907.
Wang, M., and J. E. Overland (2009), A sea ice free summer Arctic within 30 years?, *Geophys. Res. Lett.*, *36*, L07502, doi:10.1029/2009GL037820.
Westberry, T., M. J. Behrenfeld, D. A. Siegel, and E. Boss (2008), Carbon-based primary productivity modeling with vertically resolved photoacclimation, *Global Biogeochem. Cycles*, *22*, GB2024, doi:10.1029/2007GB003078.
Yool, A., E. E. Popova, and T. R. Anderson (2013a), MEDUSA–2.0: An intermediate complexity biogeochemical model of the marine carbon cycle for climate change and ocean acidification studies, *Geosci. Model Dev. Discuss.*, *6*, 1259–1365, doi:10.5194/gmdd-6-1259-2013.
Yool, A., E. E. Popova, A. C. Coward, D. Bernie, and T. R. Anderson (2013b), Climate change and ocean acidification impacts on lower trophic levels and the export of organic carbon to the deep ocean, *Biogeosciences*, *10*, 5831–5854, doi:10.5194/bg-10-5831-2013.
Zingone, A., R. Casotti, M. R. d'Alcalà, M. Scardi, and D. Marino (1995), 'St. Martin's Summer': The case of an autumn phytoplankton bloom in the Gulf of Naples (Mediterranean sea), *J. Plankton Res.*, *17*, 575–593, doi:10.1093/plankt/17.3.575.

Erratum

In the originally published version of this article, there were several instances of incorrect figures being referenced. Additionally, the color bar in Figure 6 was missing in the original version. The following have since been corrected, and this version may be considered the authoritative version of record. The first line of text on page 6 now references Figure 6. The third line of text from the bottom on page 6 now references Figure 4. The ninth line of text on page 8 now references Figure 5.